Fast motion of molecular rotors in metal–organic framework struts at very low temperature

Jacopo Perego, Silvia Bracco, Mattia Negroni, Charl Bezuidenhout, Giacomo Prando, Pietro Carretta, Angiolina Comotti,* Piero Sozzani*

Department of Materials Science, University of Milano Bicocca, Via R. Cozzi 55, 20125 Milan, Italy

and

Department of Physics, University of Pavia, Via A. Bassi 6, 27100 Pavia, Pavia, Italy

Email: piero.sozzani@unimib.it

Email: angiolina.comotti@unimib.it

The solid state is typically not well-suited to sustain fast molecular motion, but in recent years a variety of molecular machines, switches and rotors have been successfully engineered within porous crystals and on surfaces. Here we show a fast-rotating molecular rotor within the bicyclo-pentane-dicarboxylate struts of a zinc-based metal-organic framework (MOF) — the carboxylate groups anchored to the metal clusters act as an axle while the bicycle unit is free to rotate. The 3-fold bipyramidal symmetry of the rotator conflicts with the 4-fold symmetry of the struts within the cubic crystal cell of the Zn-MOF. This frustrates the formation of stable conformations, allowing for the continuous, unidirectional, hyperfast rotation of the bicycle units with an energy barrier of 6.2 calories per mole and a high frequency persistent for several turns even at very low temperatures (10^{10} Hz below 2 K). Using zirconium, instead of zinc, led to a different metal-cluster–carboxylate coordination arrangement in the resulting MOF, and a much slower rotation of the bicycle units.

Molecular-dynamics phenomena are ubiquitous in nature, and often participate in the fundamental mechanisms of living systems.[1-5] Generally, fluid phases support such phenomena while solid phases are universally considered to be the least suitable to sustain fast molecular motion. However, in solids, molecular moieties can be permanently set apart, one from the other, preventing mutual interactions and promoting unusual internal dynamics. This behavior takes place in low-density solids, such as in metal-organic frameworks (MOFs), where non-interacting moving elements can be engineered.[6-13] Dynamics in solid phases can ressemble those of liquid and gaseous phases, leading to unusual phenomena such as high thermal capacity, low surface friction and unexpected physical and chemical properties.[14,15] In recent years incorporating molecular rotors, motors and switches in the solid state have been recognized as a major challenge; recently the organization of rotating elements in the solid state or on surfaces has been shown to be an effective approach to translate their molecular dynamics into useful materials properties.[16-21]

Our group and others have been working on integrating molecular rotors into porous materials, which combine a large free-volume that promotes disentangled rotator revolution and allow chemical species to access — and intervene in — rotary mechanics.[22-28] Thus, rotor-containing porous materials provide a platform for the construction of ultra-fast reorienting elements in a robust framework. So far, a few rapid molecular rotors have been fabricated in porous frameworks by exploiting rotational axles pivoted on bonds with soft torsional barriers, such as sp^3-sp^2 and sp^2-sp bonds (Fig. 1a). This can be achieved by preventing the detrimental contributions to the rotation derived by electronic conjugation between the rotator and stator and steric crowding between ligands (Fig. 1b).[29] Indeed, rotors with high σ component on the pivotal bond or adjacent to triple bonds achieved the lowest energy barrier for rotation, and the formation of multiple conformations corresponding to shallow energy minima.[13,24] Additionally, low rotor–rotor and rotor–framework interactions have been minimized by exploiting the low density packing of the architectures.

Figure 1.

Here we have synthesized two new metal–organic frameworks (MOFs), one with zinc and the other zirconium as metal centres, both containing an aliphatic yet rigid building block bicycle-di-carboxylate linker (**1**) — the bicycle unit is the rotator and the carboxylate group acts as a stator (Fig 1c). In the zinc-based MOF, the cubic unit cell causes the planes of the two carboxylate units to arrange themselves perpendicularly (Fig. 1d). Hyperfast molecular rotor dynamics were provided by the combination of a high torsional flexibility of pivotal σ–bond (C_{sp3}-COO^-) between the bicycle unit and carboxylate moieties and the mismatch of the 3-fold trigonal symmetry of the rotating unit with the 4-fold carboxylate arrangement in the MOF (the MOFs are referred to as Zn-FTR and Zr-FTR, where FTR stands for frustrated trigonal-symmetry rotator). The torsional energy profiles on both sides of the rotator contribute out-of-phase generating geometrical frustration with a virtually flat landscape (Fig. 1e). In Zr-MOF, the crystal structure induces an in-plane conformation of the two carboxylate units (Fig. 1f), thus the rotator is surrounded by in-phase torsional barriers which sum up to form a profile with 6 minima and higher torsional barriers (Fig. 1g). The absence of either contact or long-range interactions among rotors in Zn-FTR reduces carbon–carbon torsional energy barriers to 6.2 calories per mole, lower than thermal energy even at liquid-helium temperature (RT=8.0 calories per mole at 4K). This behaviour was characterized by ^{1}H NMR; ^{1}H spin-lattice relaxation time (T_1) were recorded down to 1.5 K. Measurements of the T_1 times at distinct magnetic fields (from 0.66 to 7 Tesla) show the characteristic field-independent behaviour expected in the fast motional regime, where the dynamics are much faster than the nuclear precession frequency of 0.3 GHz at 7 Tesla. Molecular dynamics simulations gave an insight into the rotary mechanism and recognized durable runs of hyperfast unidirectional continuous rotation, rarely stopping in a single energy well.

RESULTS AND DISCUSSION

Structure of the MOF crystals. Zn-MOF was obtained by self-assembly at room temperature of the bicyclo-[1.1.1]-pentane-1,3-dicarboxylic acid ligand with Zn ions in DMF while Zr-MOF was obtained by a solvothermal synthesis modulated by formic acid to control the crystallization process. Porous crystalline architectures were obtained after gradual solvent exchange and activation under vacuum at 130° and 140 °C, respectively. Nanosize crystals of cubic and octahedral morphology were observed for Zn-FTR and Zr-FTR, respectively, as shown in SEM micrographs (Supplementary Fig. 4 and 5). The powder XRD patterns were consistent with highly ordered crystalline porous materials and the crystal structures were refined by the Rietveld method combined with molecular mechanics

and plane-wave DFT calculations (Supplementary Fig. 6,7). The crystal structure of Zn-FTR was also solved by SCXRD (Supplementary Fig. 9,10). Cubic crystal structures for Zn-FTR and Zr-FTR with space groups of F-43c and F32, respectively, were obtained (Fig. 2). The metal node in compound Zn-FTR comprises 4 zinc ions organized in tetrahedral clusters, coordinating 6 carboxylates bridging zinc pairs.[30] Comparatively, the use of Zr dramatically changes the coordinative arrangement: 12-coordinated ligands spring from the nodes, forming a crowded arrangement.[31,32] The IR spectra indicate that after coordination with Zn and Zr ions, C=O stretching bands of the carboxylate shift from 1684 cm^{-1} in the free ligand to 1609 and 1580 cm^{-1}, respectively (Supplementary Fig. 13). The number of three signals in ^{13}C MAS NMR spectra is consistent with the high symmetry of the unit cells (Supplementary Fig. 14).

Zn-FTR contains pores that can host spheres of 10.6 Å diameter, whereas Zr-FTR exhibits two smaller tetrahedral and octahedral cavities of 4.0 and 8.6 Å, as derived from the crystal structures (Figure 2c,d). The porosity of two MOFs was experimentally demonstrated by N$_2$ isotherms, displaying Langmuir type I profiles, at 77 K (Supplementary Fig. 16,17). The Zn-FTR material was found to exhibit a surface area of 2,700 m^2/g and a pore volume of 1.17 cm^3/g, with a pore size distribution centred at 11.8 Å, in reasonable agreement with the pore sizes from the crystal structures. In the case of Zr-FTR, a surface area of 1,020 m^2/g and a pore volume of 0.45 cm^3/g were determined. The pore size distribution showed a peak centered at 8.5 Å which corresponded to the diameter of the larger pore while the smaller pores are not detectable by N$_2$ adsorption isotherm.

In the crystal structure of the Zn-FTR material, the three methylenes of the bi-cyclopentane rotator lie on a common plane arranged as a wheel mounted on the main molecular axis of the ligand (Fig. 2e): any wheels in Zn-FTR set their hydrogen atoms at distances of 7.9 Å and 5.4 Å from the next neighbouring rotor hydrogens. Consequently, they do not interfere with each other or with any other moiety in the rotary dynamics. The distances are shorter among the rotors in Zr-FTR (3.3 Å), but are still longer than the van der Waals contacts (Fig. 2f).

Figure 2.

Rotor conformations and energy landscape. A key point of the MOF crystal structure is that the carboxylate planes in Zn-FTR are set perpendicular to one another (crossed arrangement) while in Zr-FTR the carboxylate groups lie on a common plane (in-plane arrangement) (Figure 3a,b). Both arrangements of the carboxylate end-groups have been reported in the literature and depend on the nature of ligands and metal ions: for example in MOF-5 the important contribution of the electronic conjugation with the aromatic ring determines the in-plane arrangement (see also Supplementary Fig.

21 and Table 10). *Ab initio* conformational analysis of the dicarboxylate-bicyclopentane showed the crossed arrangement as more stable by 0.39 kcal/mol than the in-plane arrangement (Supplementary Fig. 18): however, the anchorage of the ligands to the metal nodes prevents conversion between arrangements in the structures. These arrangements have dramatic consequences on the energetics of the central rotator. The torsional conformations were investigated by MP2 potential energy scans, displaying minima every 60° (sixfold rotation axis) for the in-plane arrangement, while the energy minima occurred with a period of 30° (twelvefold rotation axis) for the crossed arrangement (Fig. 3c,d). In both cases the energy barriers, as calculated by MP2/6-311+G(d), are of a few calories per mole. The energy barrier of in-plane conformation is accounted for 50 cal mol^{-1}, while in crossed arrangement it was found to be lower than a few calories per mole and comparable to the thermal agitation at 0.5 K (Fig. 3e), showing the extremely-high torsional flexibility of the rotator, comparable to methyl rotation flexibility.[33-36]

Figure 3.

To rationalize the energy profiles in the two distinct conformations, and how the nearly degenerate states occur in the crossed arrangement, it must be considered that the rotor interacts periodically with both adjacent carboxylates on opposite sides of the rotor plane — that is, the plane perpendicular to the main axis of the ligand. The energy profile for the interaction of the rotor with each carboxylate generates six minima, consistent with the combination of two-fold and three-fold symmetries of the carboxylates and the rotor, respectively. The total energy potential is then composed by a summation of the two potentials generated by the rotation of bicyclo moiety with respect to the two planes of the carboxylate groups lying on both sides (Fig. 3 f,g). In the in-plane conformation the two potentials are in-phase ('constructive interference'), so that the profile is retained and intensified. On the contrary, in the crossed conformation, the two periodic functions are shifted by half a period and are out of phase; thus the proper mismatch of the added potentials produces the observed 'destructive interference', and the rotor is frustrated in its tendency to fall in deep minima.

Rotor dynamics. An effective tool to provide the evidence of dynamics in crystalline matter is variable-temperature solid-state NMR spectroscopy. ^{13}C NMR spectra of Zn-FTR, recorded under static conditions which would potentially highlight the anisotropic profile, exhibited pseudo-isotropic signals for methylenes, both at room temperature and down to 163 K. The spectra of Zn-FTR and Zr-FTR showed narrow lines with width of 1.4 and 2 ppm, respectively, depicting a rotary revolution that is fast enough to average out chemical-shift-anisotropy (CSA) (Fig. 4a, red lines).[37] For comparison, Fig. 4a shows the full CSA profile determined by *ab initio* GIAO calculations (dashed black line), consistent with the reference bicyclopentane hydrocarbon CSA. The mixing of the

principal tensor-components in the x-y plane orthogonal to the rotor axis (σ_{xx} = 44 ppm and σ_{yy} = 60 ppm, Fig. 4b) produces an averaged value of 52 ppm, equal to the σ_{zz} component, which is unaffected by rotator reorientation, being parallel to the rotation axis. This restriction of CSA to isotropic lines in the solid state is of the same order of magnitude than that in globular molecules, such as adamantane and fullerene, which display linewidths of 5 ppm at 298 K and of 2.4 ppm at 190 K, respectively — although in these cases phase transitions prevent fast dynamics at lower temperatures.[38,39] For comparison, at 163 K the sterically hindered Zr-MOF showed a residual CSA profile and a 4.4 ppm linewidth, with a prominent peak corresponding to the mixing of σ_{xx} and σ_{yy}, and a lateral signal for the σ_{zz} component (Fig. 4c, green line). The identification of an σ_{zz} separate component, not mixed with the remaining tensors, clearly highlights the axial symmetry of the rotary trajectories.

Solid-state ^{1}H-NMR spectra of Zn-FTR displayed 10 kHz-wide methylene signals (Fig. 4d), which appear markedly modulated by through-space homonuclear dipolar couplings even at 2 K. The unusual ^{1}H NMR spectrum patterning was successfully simulated by considering the orientation and distance dependence of the dipole–dipole interactions in the 6-spin cluster of an individual rotor under magnetic and molecular isolation. The spectra are substantially a combination of "Pake" patterns (characteristic lineshapes from dipolar couplings) containing the anisotropic information and dynamical averaging among hydrogens in the rotator plane (Supplementary Fig. 23). A similar 6-nuclei modulated spectrum has only been investigated in fast-spinning benzene within a graphite layer.[40] An orbital trajectory of hydrogen nuclei, perpendicular to the rotor main axis in the fast motion limit ($>10^8$ Hz), was demonstrated by the overall line-shape restriction of the full 'static' powder pattern to be half of its width. Furthermore, taking into account hydrogen–hydrogen dipolar interactions in the crystal cell, we evaluated the second moment and demonstrated that 98% of the effective interactions occur within the six methylene hydrogens of each rotator (Fig. 4d and Supplementary Fig. 24).[41] Importantly, from this evaluation it was possible to calculate the relaxation constant C of $5.8*10^9$ s^{-2} (proportional to the mean square amplitude of the fluctuating field at the nuclei), which is used below to establish the correlation times from NMR spin-lattice relaxation times.

Figure 4.

Solid-state NMR relaxation times enable the exploration of material dynamics and, collected at various resonance frequencies, give access to reorientation rates of several orders of magnitude. ^{1}H T_1 relaxation times of the bicyclopentane methylenes in Zn-FTR were measured from 298 K down to 1.5 K at a few distinct main magnetic fields B_0 equal to 7.04, 1.66, 1.00 and 0.66 T (Fig. 4e: 70 points

were collected). The relaxation times were plotted as $\ln T_1$ vs $1/T$ and fitted by the universal master-curve, according to the Kubo–Tomita theory (K–T).[42] Such a plot exhibited a field-independent linear decrease with inverse temperature and a constant slope over the entire range (Fig. 4e; the 77-298 K range is expanded for clarity). This indicates that the relaxation times are determined by dynamics much faster than the nuclear Larmor frequency, even at extremely low temperature. The barrier for rotation resulted in a value as low as 6.2 cal mol^{-1} (26 J mol^{-1}) for Zn-FTR. Muon spin-relaxation experiments support the extremely low energy barrier (Supplementary Section 2.17). The very low activation-energy value supports the almost negligible energy barriers for rotation in this molecular rotor. By taking into account the previously determined relaxation constant C, the correlation times can be established for each temperature. Importantly, the correlation time at 'infinite' temperature τ_0 of $4*10^{-12}$ s is consistent with the theoretical value of $4.2*10^{-12}$ s, as derived from the potential of the rotating system of 42 mass-units (3 carbons plus 6 hydrogens, moment of inertia of $8.23*10^{-22}$ Kg m^2 mol^{-1}) (Supplementary Section 1.2).[43] This adds further support to our assignment that the bicyclo 'molecular wheels' in Zn-FTR operate as individual rotating entities, independent from each other. Hyper-fast rotary motion of $k=37$ GHz ($1/\tau_c=2.3*10^{11}$ s^{-1}) at room temperature, and still in the GigaHertz regime ($k=7.9*10^9$ Hz and $1/\tau_c=5.0*10^{10}$ s^{-1}) at temperatures as low as 2 K was established. Such a low energy-barrier of rotary dynamics allows $k=7.3*10^7$ Hz ($1/\tau_c=4.5*10^8$ s^{-1}) rotation to occur at a temperature as low as 0.5 K. To the best of our knowledge, fast molecular rotors in organic matter have not been observed at the liquid helium temperature and below, because the energy barrier is prohibitively high for thermal energy to compete and quenches the rotation (less than 1 Hertz).[13,24] Unlike other examples reported in the literature, 'unrestricted' motion for the entire temperature range (2 K – 300 K) was achieved with a relatively large inertial mass. No evidence for slope change at low temperature, which may indicate a regime of tunneling,[43,44] is observed in the spin–lattice relaxation times. The dynamics shown here are approaching the fastest rotation speed among organic moieties at low temperature, such as methyl groups, in the solid and even in the gas phase.[45-46] The low rotation barrier determined suggests that the rotor symmetry frustration obtained in the MOF host ensures high 'mechanical' flexibility.

Modulation of rotor speed. The observation of the same bicyclopentane rotor in the sterically hindered Zr-FTR structure, which imposes a diverse symmetry and density, could probe the effect of the crystal environment on the rotor freedom, yielding a higher energy barrier of 400 cal mol^{-1} for rotation (Supplementary Fig. 32). In fact, shorter distances between the rotors (3.3 Å) in Zr-FTR are observed.

In addition, modulation of the rotation speed was achieved under chemical stimuli in porous Zn-FTR by the introduction of a gaseous species (I_2), which interacts with the rotors accessible through the open pores. Indeed, in the presence of I_2 molecules diffusing spontaneously into the porous crystals at 27 mbar vapour pressure, at 293 K, the rotary speed was drastically reduced. It was still however in the fast motion regime: the energy barrier increased to 1000 cal mol^{-1}, that is, three orders of magnitude larger than the empty (guest-free) matrix (Supplementary Fig. 32). This increased activation energy from a negligible value was ascribed to a 'weak' favourable interaction of the C-H peripheral methylenes of the rotor-wheel, exposed to the empty volume with iodine molecules, thus probing the sensitivity of the material for any minimal perturbation, useful as a prompt and reversible detector.

Molecular dynamics simulations. Molecular dynamics simulations helped provide a deeper insight into the functioning of molecular rotors (Fig. 5). The rotor dynamics was determined by analysing the evolution of the rotatory torsion angles with respect to time of three rotators selected as representative of the entire population for each compound (Supplementary Fig. 36). In both compounds the rotor axis oscillations (nutation) are not larger than 3° at any temperature (Supplementary Fig. 33). The robustness of the double anchorage (the carboxylate groups on either side of the bicyclo rotating moiety) firmly supports the axle to the framework, unlike a methyl rotor, which is mono-dentate and is thus pivoted only on one side.[35,46] The cumulative angular displacement of the rotors at room temperature, shown in number of turns, is depicted in Fig. 5b for the three selected rotators in Zn-FTR. Clockwise or counter-clockwise rotation can be differentiated by positive or negative angular displacement.

Figure 5.

A first observation was that the rotator neither resides in a single energy minimum, oscillating therein, nor does it move stepwise by jumping from one minimum to the next. Conversely, a multiple-turn displacement, overflying a large number of energy minima (up to 4000 minima, 12 minima are equal to 1 turn), was observed. The molecular wheel appears to spin freely and performs a diffusional motion, overriding negligible minima for up to 500 continuous unidirectional revolutions in either clockwise or counter-clockwise directions depicting a waving behavior as shown in Figure 5b and c. By representing the rotation angles explored by an individual rotator in a 0° - 360° scale against time, the signature of the continuous motion becomes imprinted as parallel noiseless lines (Fig. 5d). Chaotic thermal energy is higher than the activation energy for rotation but, at the same time, the 42-dalton rotational mass of the rotor is sufficiently high to ensure the unusual conservation of rotational

momentum for a certain period of time. Indeed, such inertial behavior combined with flat energy profile allow for continuous unidirectional motion which lasts for as long as 0.5 nanoseconds at room temperature. The rotary speed can be sampled by the average slope (the derivative of the cumulative angle versus time) over several turns in a lasting continuous rotation, and was as fast as $4.5 \cdot 10^{11}$ Hz (Fig. 5b,c). This value is in very good agreement with the correlation time τ_0 of $4.3*10^{-12}$ s measured experimentally by NMR relaxation and Kubo–Tomita analysis.

At low temperature, the rotators possess lower thermal energy and can be trapped occasionally in potential energy wells (Fig. 5e). The rapid intermittent stop-and-go behaviour and the persistence at low temperature of hyper-fast rotation manifested in continuous unidirectional motion (Figure 5f,g), suggest that the rotator explores energetic states higher than the tiny energy barrier, even at 2.5 K. The direction can be easily recognized in each free-rotation packet by the positive or negative inclination of the parallel lines. By comparison, Zr-FTR, characterized by a higher barrier, shows frequently-occurring conventional jumps from one energy-well to the next one (Supplementary Fig. 41,42,48).

Conclusion

In conclusion, we have realized a fast molecular rotor in the solid state whose rotation speed approaches that of unhindered rotations in organic moieties, and was shown to be faster than methyl rotation even at very low temperatures (2 K). The bicyclo-pentane rotors were hosted within the struts of a low-density porous crystalline metal–organic framework and energetically decoupled from their surroundings. The rotors, isolated from one another in the high-symmetry structure, showed a negligible torsional barrier to rotation. A key point was the unusual crossed conformation adopted by the carboxylates around the pivotal bond on the rotor axle, generating a 4-fold symmetry that does not match the 3-fold rotation symmetry of the rotor. This produced geometrical frustration and, for a full turn, 12 very shallow wells along the circular trajectory.

This behaviour is the result of the continuous unhindered molecular wheel rotation for several turns, rather than the jumping motion usually observed for barrier-restricted rotations. The present system demonstrates the existence of dynamic materials under very low temperatures, perhaps suggesting future investigations into regular arrays of rotary motors and rotors showing enhanced performance under low thermal perturbation conditions. Actually, molecular motors and switches must compete with thermal noise, which interferes with their coherent functioning. Temperature reduction to the lowest limit can be envisaged to minimize the disturbance of thermal energy and perform coherent task. However, this reduction generally hinders molecular dynamics. Instead, fast molecular motors

and switches can extend their working range, provided that the torsional barriers are sufficiently lower than thermal energy, even at low temperature.

References

1. Saibil, H. Chaperone machines for protein folding, unfolding and disaggregation. *Nat. Rev. Mol. Cell Biol.* **14**, 630-642 (2013).
2. Kinbara, K. & Aida, T. Towards intelligent molecular machines: Directed motions of biological and artificial molecules and assemblies. *Chem. Rev.* **105**, 1377-1400 (2005).
3. Olesen, C. et al. The structural basis of calcium transport by the calcium pump. *Nature* **450**, 1036-1042 (2007).
4. Howard, J., Hudspeth, A. J. & Vale, R.D. Movement of microtubules by single kinesin molecules. *Nature* **342**, 154-158 (1989).
5. Preben Morth, J., Pedersen, B. P., Andersen, J. P., Vilsen, B., Palmgren, M. G. & Nissen, P. A structural overview of the plasma membrane Na^+,K^+-ATPase and H^+-ATPase ion pumps. *Nat. Rev. Mol. Cell Biology* **12**, 60–70 (2011).
6. Vogelsberg, C. S. & Garcia-Garibay, M. A. Crystalline molecular machines: function, phase order, dimensionality, and composition. *Chem. Soc. Rev.* **41**, 1892-1910 (2012).
7. Bracco, S., Comotti, A. & Sozzani, P. Molecular rotors built in porous materials. *Acc. Chem. Res.* **49**, 1701-1710 (2016).
8. Danowski, W. et al. Unidirectional rotary motion in a metal-organic framework. *Nat. Nanotech.* **488**, 488-494 (2019).
9. Deng, H., Olson, M. A., Stoddart, J. F. & Yaghi, O. M. Robust dynamics. *Nat. Chem.* **2**, 439-443 (2010).
10. Zhu, K., O'Keefe, C. A., Vukotic, V. N., Schurko, R. W. & Loeb, S. J. A molecular shuttle that operates inside a metal-organic framework. *Nat. Chem.* **7**, 514-519 (2015).
11. Kobr, L. et al. Inclusion Compound Based Approach to Arrays of Artificial Dipolar Molecular Rotors. A Surface Inclusion. *J. Am. Chem. Soc.* **134**, 10122-10131 (2012).
12. Inukai, M., Fukushima, T., Hijikata, Y., Ogiwara, N., Horike, S. & Kitagawa, S. Control of Molecular Rotor Rotational Frequencies in Porous Coordination Polymers Using a Solid-Solution Approach. *J. Am. Chem. Soc.* **137**, 12183-12186 (2015).
13. Vogelsberg, C. S. et al. Ultrafast rotation in an amphidynamic crystalline metal organic framework. *Proc. Natl Acad. Sci. USA* **114**, 13613-13618 (2017).
14. Michl, J., Charles, E. & Sykes, H. Molecular Rotors and Motors: Recent Advances and Future Challenges. *ACS Nano* **3**, 1042-1048 (2009).
15. Prokop, A., Vacek, J. & Michl, J. Friction in carborane-based molecular rotors driven by gas flow or electric field: classical molecular dynamics. *ACS Nano* **6**, 1901-1914 (2012).
16. Coskun, A., Banaszak, M., Astumian, R. D., Stoddart, J. F. & Grzybowski, B. A. Great expectations: can artificial molecular machines deliver on their promise? *Chem. Soc. Rev.* **41**, 19-30 (2012).
17. Steuerman, D. W., Tseng, H.-R., Peters, A. J., Flood, A. H., Jeppesen, J. O., Nielsen, K. A., Stoddart, J. F. & Heath, J. R. Molecular-Mechanical Switch-Based Solid-State Electrochromic Devices. *Angew. Chem. Int. Ed.* **43**, 6486-6491 (2004).
18. Collier, C. P., Mattersteig, G., Wong, E. W., Luo, Y., Beverly, K., Sampaio, J., Raymo, F. M., Stoddart, J. F. & Heath, J. R. A [2]Catenane-Based Solid State Electronically Reconfigurable Switch. *Science* **289**, 1172-1175 (2000).
19. Kaleta, J. et al. Surface Inclusion of Unidirectional Molecular Motors in Hexagonal Tris(o-phenylene) cyclotriphosphazene. *J. Am. Chem. Soc.* **139**, 10486-10498 (2017).

20. Jiang, X. et al. Crystal Fluidity Reflected by Fast Rotational Motion at the Core, Branches, and Peripheral Aromatic Groups of a Dendrimeric Molecular Rotor. *J. Am. Chem. Soc.* **138**, 4650-4656 (2016).

21. Comotti, A., Bracco, S., Ben, T., Qiu, S. & Sozzani, P. Molecular Rotors in Porous Organic Frameworks. *Angew. Chem. Int. Ed.* **53**, 1043-1047 (2014).

22. Comotti, A., Bracco, S., Yamamoto, A., Beretta, M., Kirukawa, T. Tohnai, N. Miyata, M. & Sozzani, P. Engineering Switchable Rotors in Molecular Crystals with Open Porosity. *J. Am. Chem. Soc.* **136**, 618-621 (2014).

23. Bracco, S. et al. CO_2 regulates molecular rotor dynamics in porous materials. *Chem. Commun.* **53**, 7776-7779 (2017).

24. Bracco, S. et al. Ultrafast molecular rotors and their CO_2 tuning in MOFs with rod-like ligands. *Chem. Eur. J.* **23**, 11210-11215 (2017).

25. Bracco, S., Beretta, M., Cattaneo, A., Comotti, A., Falqui, A., Zhao, K., Rogers, C. & Sozzani, P. Dipolar Rotors Orderly Aligned in Mesoporous Fluorinated Organosilica Architectures. *Angew. Chem. Int. Ed.* **54**, 4773-4777 (2015).

26. Horike, S., Matsuda, R., Tanaka, D., Matsubara, S., Mizuno, M., Endo, K. & Kitagawa, S. Dynamic Motion of Building Blocks in Porous Coordination Polymers. *Angew. Chem., Int. Ed.* **45**, 7226-7230 (2006).

27. Zhu, K., Vukotic, V. N., Okeefe, C. A., Schurko, R. W. & Loeb, S. J. Metal–organic frameworks with mechanically interlocked pillars: controlling ring dynamics in the solid-state via a reversible phase change. *J. Am. Chem. Soc.* **136**, 7403–7409 (2014).

28. Elsaidi, S.K., Mohamed, M. H., Simon, C. M., Braun, E., Pham, T., Forrest, K. A., Xu, W., Banerjee, D., Space, B., Zaworotko, M. J. & Thallapally, P. K. Effect of ring rotation upon gas adsorption in SIFSIX-3-M (M = Fe, Ni) pillared square grid networks. *Chem. Sci.* **8**, 2373-2380 (2017).

29. Gonzalez-Nelson, A., Coudert, F.X. & van der Veen, M. Rotational dynamics of linkers in metal-organic frameworks. *Nanomaterials* **9**, 330-366 (2019).

30. Li, H., Eddaoudi, M., O'Keeffe, M. & Yaghi, O. M. Design and synthesis of an exceptionally stable and highly porous metal-organic framework. *Nature* **402**, 276-279 (1999).

31. Cavka, J. H., Jakobsen, S., Olsbye, U., Guillou, N., Lamberti, C., Bordiga, S. & Lillerud, K. P. A New Zirconium Inorganic Building Brick Forming Metal Organic Frameworks with Exceptional Stability. *J. Am. Chem. Soc.* **130**, 13850–13851 (2008).

32. Yuan, S., Qin, J.-S., Lollar, C. T. & Zhou, H.-C. Stable Metal−Organic Frameworks with Group 4 Metals: Current Status and Trends. *ACS Cent. Sci.* **4**, 440-450 (2018).

33. Owen, N. L. in Internal Rotation in Molecules. Ed. Orville-Thomas, W. J. (Wiley, New York, 1974), p. 157.

34. Nakagawa, J. & Hayashi, M. Microwave spectrum and internal rotation of 2-butyne-1, 1, 1-d_3(dimethylacetylene), $CH_3C \equiv CCD_3$. *J. Chem. Phys.* 80, 5922-5925 (1984).

35. Ilyushin, V., Rizzato, R., Evangelisti, L., Feng, G., Maris, A., Melandri, S. & Caminati, W. Almost free methyl top internal rotation: Rotational spectrum of 2-butynoic acid. *J. Mol Spectr.* **267**, 186-190 (2011).

36. Hensel, K. D. & Gerry, M. C. L. Microwave spectrum of tetrolyl fluoride. *J. Chem. Soc. Farad. Trans.* **90**, 3023 (1994).

37. Facelli, J. C., Orendt, A. M., Beeler, A. J., Solum, M. S., Depke, G., Malsch, K. D., Downing, J. W., Murthy, P. S., Grant, D. M. & Michl, J. Low-temperature carbon-13 magnetic resonance in solids. 5. Chemical shielding anisotropy of the $^{13}CH_2$ group. *J. Am. Chem. Soc.* **107**, 6749, 6754 (1985).

38. Gil, A.M. & Alberti, E. The effect of Magic Angle Spinning on proton spin–lattice relaxation times in some organic solids. *Solid State Nuclear Magnetic Resonance.* **11**, 203-209 (1998).

39. Ticko, R., Dabbagh, G., Fleming, R. M., Haddon, R. C., Makhjia, A. V. & Zahurak, S. M. Molecular dynamics and the phase transition in solid C60. *Phys. Rev. Lett.* **67**, 1886-1889 (1991).
40. Panich, A. M. & Panich, E. A. NMR Lineshape of a Six-Spin System with Dipole-Dipole Interactions. Application to Benzene. *J. Magn. Res. Series A* **116**, 113-116 (1995).
41. Goc, R. Computer calculation of the Van Vleck second moment for materials with internal rotation of spin groups. *Comp. Phys. Comm.* **162**, 102-112 (2004).
42. Kubo, R. & Tomita, K. A General Theory of Magnetic Resonance Adsorption. *J. Phys. Soc. J.* **9**, 888-919 (1954).
43. Koksal, F. & Rossler, E. Spin-lattice relaxation by tunneling motions of methyl groups in some organic compounds. *Solid State Comm.* **44**, 233-235 (1982).
44. Layanowicz, L. Spin-lattice NMR relaxation and second moment of NMR line in solids containing CH3 groups. *Concepts in Magnetic Resonance*, **44A**, 214–225 (2015).
45. Noel L. Owen, in Internal Rotation in Molecules, edited by W. J. Orville-Thomas (Wiley, New York, 1974), p. 157.
46. Eibl, K., Kannengießer, R., Stahl, W., Nguyen, H. V. L. & Kleiner, I. Low barrier methyl rotation in 3-pentyn-1-ol as observed by microwave spectroscopy. *Molecular Phys.* **114**, 3483-3489 (2016).

Acknowledgements

Author Contributions

A.C., P.S. conceived the study, J.P. designed the materials synthesis and characterization, S.B., G.P., M.N., P. C. carried out NMR measurements and C.B. the theoretical calculations. A.C., P.S. and S.B. co-wrote the manuscript with the suggestions from all the authors. I. Supino is acknowledged for her help during sample preparation.

Corresponding author

Correspondence to Piero Sozzani (piero.sozzani@unimib.it).

Competing Interests

The authors declare no competing interests.

Additional information

Supplementary information is available for this paper.
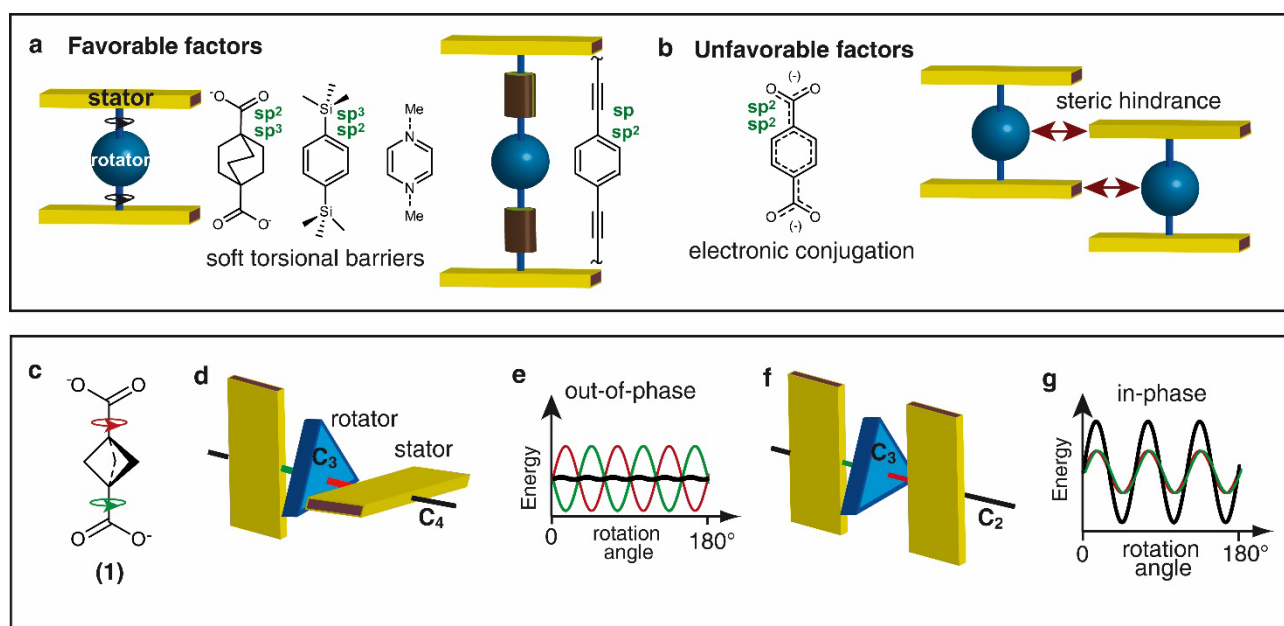
Figure Legends

Fig. 1. Factors influencing the molecular rotor dynamics, conformations of the rotator and stator in the ligand and the resulting energy profiles. (**a**) Ligands containing molecular rotors with soft pivotal bonds (sp^3-sp^2 and sp^2-sp bonds) along the rotor axles. (**b**) Electronic conjugation (sp^2-sp^2 bonds) within the ligand and intermolecular steric crowding influencing negatively rotor dynamics. (**c**) Chemical structure of bicyclo-[1.1.1]-pentane-1,3-dicarboxylate ligand (**1**). (**d,f**) Sketch of the ligand conformation highlighting the symmetry of both the rotator and stator. Dicarboxylate planes, as depicted by yellow parallelepipeds, are arranged perpendicular and parallel to each other. The blue triangles represent the bicyclo rotator. Individual torsional energy profiles about the bonds connecting the rotator to the stators (green and red colors) contributing out-of-phase to form an almost flat total energy profile (black line) (**e**) and in-phase to increase energy barriers (**g**).
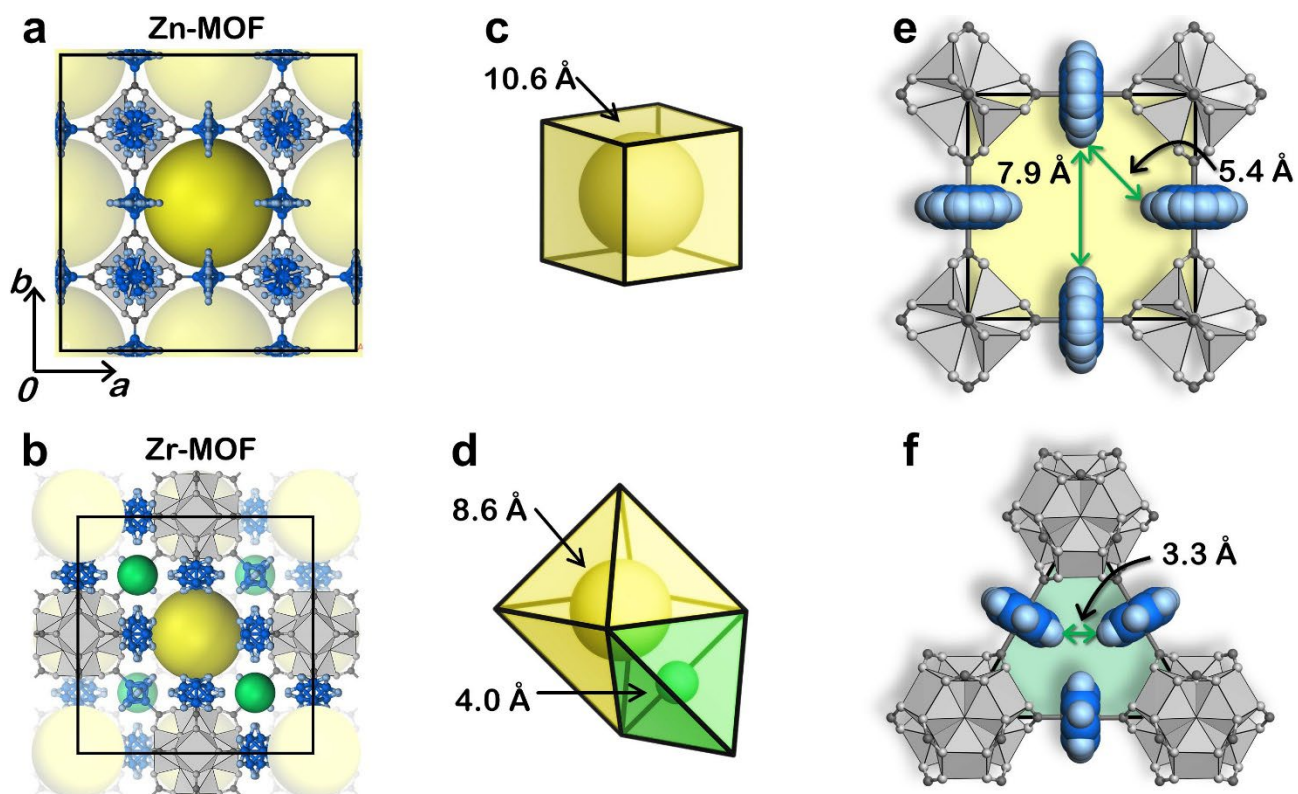
Fig. 2. Crystal structure, cavity geometry and rotors in the frameworks. (**a,b**) The crystal structures of Zn-MOF and Zr-MOF viewed along the *c*-axis. The metal-oxide nodes are shown in the polyhedron representation (metal nodes: grey, carbons: light blue and hydrogens: white). (**c,d**) The schematic geometries of the pores for both MOFs as well as the largest spheres that can be accommodated within the pores. The diameters of the spheres, indicated in the figure, were based considering the van der Waals radii of the host atoms. (**e,f**) View showing the shortest distances between the rotor hydrogen atoms, as calculated from the center of the nuclei for Zn-FTR (**e**) and Zr-FTR (**f**).
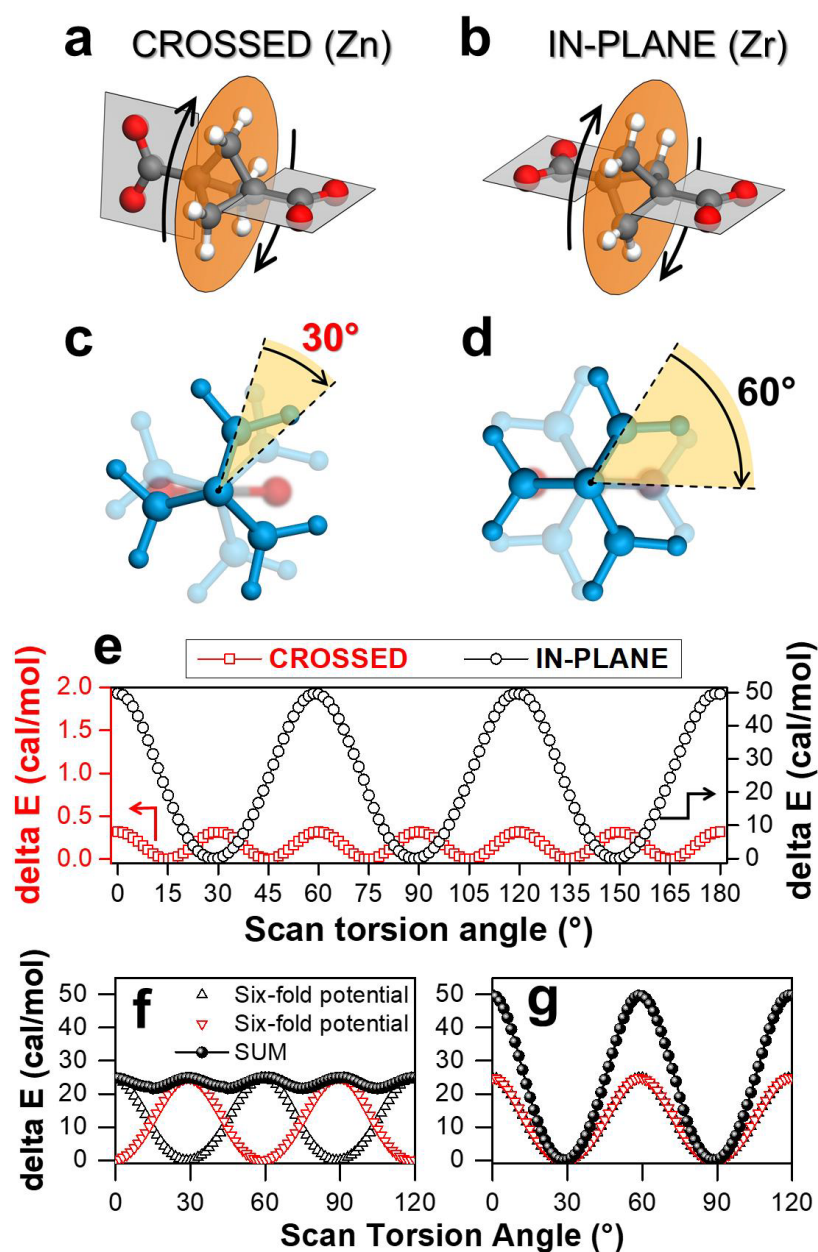
Fig. 3. Crossed(Zn) and in-plane(Zr) conformations with torsional energy profiles of the ligands. (a,b) Rotor minimum conformations for crossed and in-plane arrangements as in Zn-FTR and Zr-FTR, respectively. **(c,d)** Conformational minima for the crossed and in-plane arrangements occurring by rotations of 30° and 60°, respectively. **e** An overlay of the crossed (red squares) and in-plane (black circles) potential energy scans (PES) plotted from 0 to 180° with separate y-axes scales (crossed on the left in red and in-plane on the right in black). **(f,g)** Six-fold torsional potential of the rotator about the C-C bond with each carboxylate moiety (black and red triangles) for out-of phase and in-phase conformations, respectively. The mathematical summation of two 6-fold potentials for the out-of-phase and in-phase are represented as black spheres. In the case of out-of-phase summation the mismatch of the potentials led to a substantial compensation (crossed conformation, 12 minima); in the case of in-phase summation the the profile is retained and intensified (in-plane conformation, 6 minima).
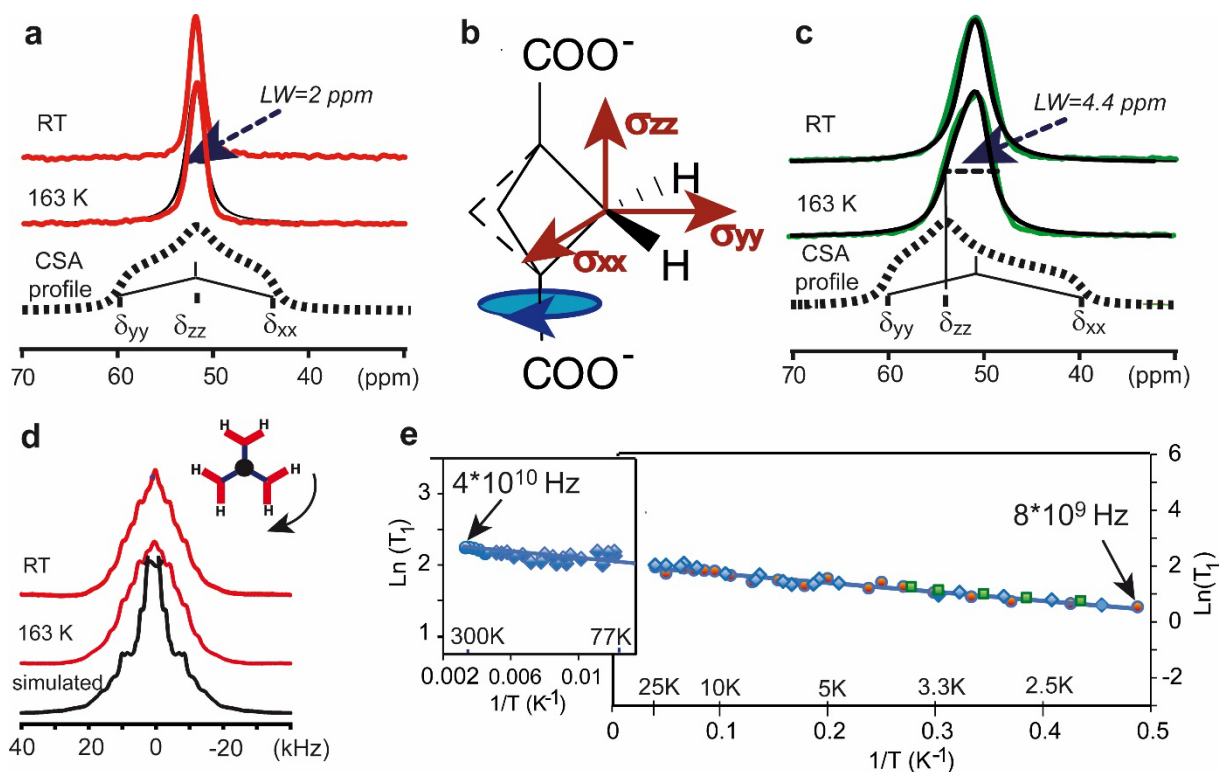
Fig. 4. Solid state NMR spectra and ^1H T_1 spin-lattice relaxation times of the molecular rotor in the MOFs recorded at various magnetic fields. (a,c) ^{13}C CP MAS NMR spectra of Zn-FTR (red) and Zr-FTR (green) **(c)** at room temperature, at 163 K and restricted CSA profiles (black) calculated by considering fast rotation of CH_2 about their main axis. Full theoretical CSA profiles (dashed lines) **(b)** Chemical structure of dicarboxylate-bicyclopentane and the main components of the ^{13}C CSA tensor. **(d)** ^1H solid state NMR spectrum of Zn-FTR collected under static conditions at room temperature, at 163 K (red) and the simulated pattern (black) obtained from the dipolar couplings among a cluster of six hydrogens, as in an isolated bicyclo-based molecule. **(e)** Ln $T_1(^1H)$ relaxation times versus the reciprocal of temperature in the temperature range from 1.5 to 300 K. The T_1 relaxation times were measured at 7.04 (blue circle), 1.66 (green square), 1.0 (blue diamond) and 0.66 T (orange circle).
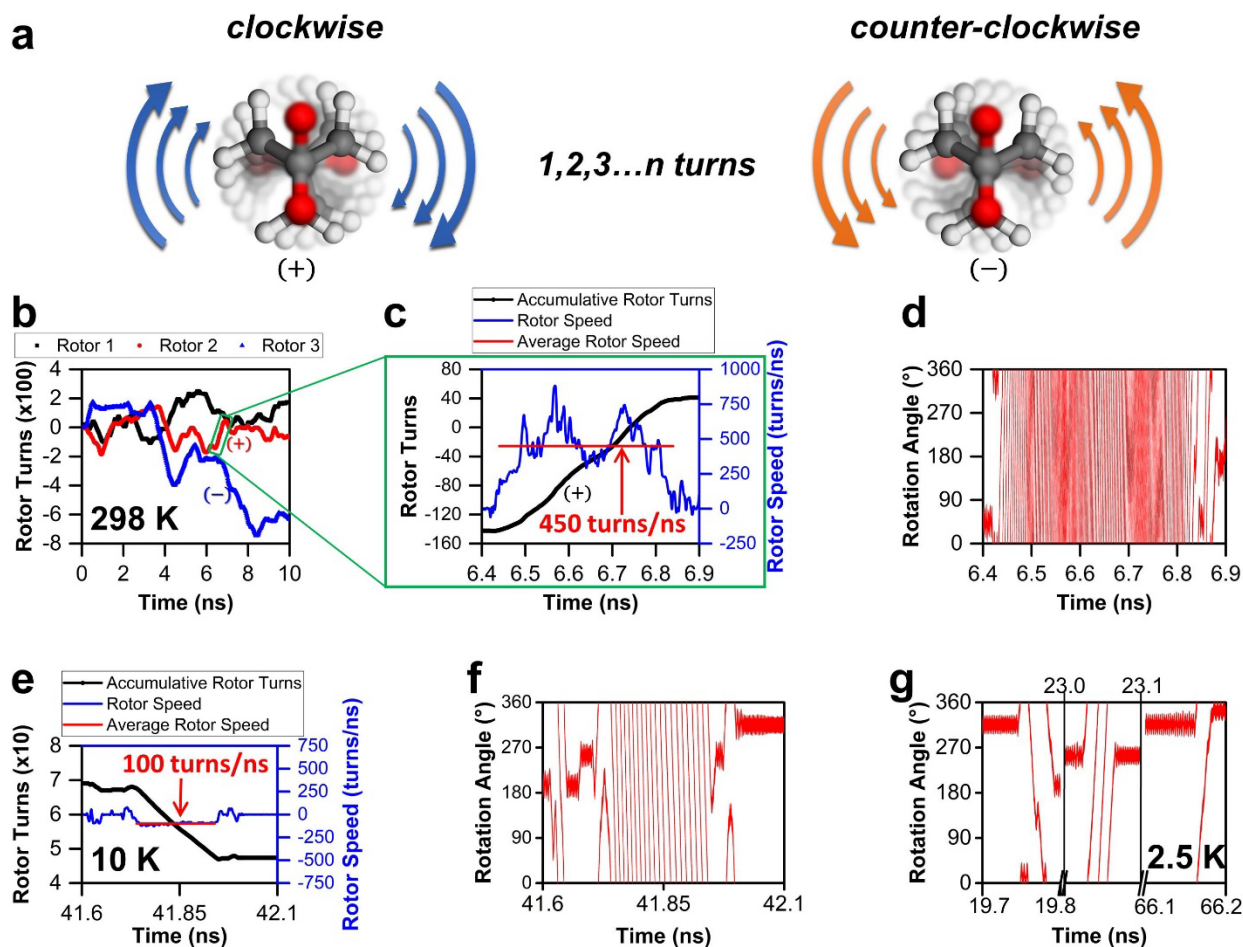
Fig. 5. Molecular Dynamics results for Zn-FTR calculated at various temperatures. (**a**) An illustration of clockwise and counter-clockwise rotation of the bicyclo rotating moiety showing the multiple turns performed in a single direction. (carbon: grey and oxygen: red) (**b**) The time evolution of the cumulative torsion angular displacement at 298 K, reported as number of turns starting from an arbitrary zero configuration of three selected rotators, clockwise or counter-clockwise rotation is indicated by positive or negative signs. (**c**) An enlarged section (0.5 ns) of the 298 K dynamics simulation highlighting a continuous unidirectional rotation for 225 turns (black line), the associated angular speed (blue line) and the average speed (red line), espressed as number of turns per nanosecond. (**d**) The 298 K rotator angular displacement represented in a 0° – 360° scale for the 0.5 ns time window. (**e**) A section of the 10 K dynamics simulation highlighting a continuous unidirectional movement (black line), the associated angular speed (blue line) and the average speed (red line) during a 0.5 ns time period. (**f**) The 10 K rotator angular displacement represented in a 0° – 360° scale. (**g**) The 2.5 K rotator angular displacement represented in a 0° – 360° scale showing different time windows of the dynamics simulation.

Methods

Synthesis of Zn-FTR. A solution of $Zn(CH_3COO)_2 \cdot 2H_2O$ (197.56 mg; 0.90 mmol) in dry N,N'DMF (3 ml) was added dropwise to a solution of 1,3-bicyclo[1.1.1]pentanedicarboxylic acid (**1**) (46.84 mg; 0.30 mmol) in dry N,N'-DMF (3 ml) over a period of 5 minutes at room temperature under stirring. The mixture was additionally stirred for 30 minutes and then left under static conditions for 16h. The white precipitate is centrifuged and fresh dry DMF was replaced 4 times (4x5ml). The solvent was exchanged and soaked in dry DCM for 2 days replacing the solvent two times a day. The material was activated in high vacuum at room temperature for 8h and then at 130°C overnight. The sample is stable under inert atmosphere, e.g. N_2 atmosphere, and at low relative humidity (RH $\leq$ 0.3) it is stable for several hours.

Synthesis of Zr-FTR. $ZrCl_4$ (144.6 mg; 0.62 mmol) and 1,3-Bicyclo[1.1.1]pentanedicarboxylic acid (**1**) (290.4 mg; 1.86 mmol) were dispersed in a mixture of dry DMF (24 ml) and formic acid (456 µl; 12 mmol) in a 100 ml glass vial and the mixture was sonicated for 1 minutes at room temperature and then heated at 120 °C for 22 h. Then, the vial is taken out of the oven and cooled at room temperature. The white solid is filtered on a 0.2 µm PTFE filter and washed with DMF (100 ml) and methanol (100 ml). The resulting powder was activated in high vacuum first at room temperature and then at 140°C overnight.

I_2 loading in Zn-FTR. The sample Zn-FTR (57 mg) inside a 2.5 ml glass vial was inserted in a Schlenk tube and treated at 130°C under high vacuum overnight. After cooling to room temperature, the sample was exposed to iodine vapors for 72 h in static vacuum conditions. Finally, the iodine source was disconnected and the iodine loaded sample (I_2@Zn-FTR) was analysed with multiple techniques (Infrared spectroscopy, PXRD and solid state NMR).

Solution ^{1}H NMR. ^{1}H-NMR spectra were recorded on a 500 MHz Bruker instruments. Chemical shifts are reported in ppm.

Infrared spectroscopy. Infrared spectra measurements were performed with a Jasco FT/IR 4100 equipped with an ATR PRO450-S module. The samples were evacuated under high vacuum at 130 °C (Zn-FTR) and 140 °C (Zr-FTR) before analysis to ensure the complete removal of adsorbed water vapour and guest species. Spectra were collected in transmission mode between 600 and 4000 cm^{-1} with a resolution of 2.0 cm^{-1}.

Micro-infrared (Micro-FTIR) spectrum was measured on a Nicolet™ iN™10 Infrared Microscope (Thermo Fisher Scientific) equipped with a liquid nitrogen cooled detector working in reflection conditions. The sample was degassed at 140°C for 12 hours before the measurement and quickly deposited on a gold substrate for analysis. The spectrum was collected with a resolution of 4 cm -1 between 600 and 4000 cm^{-1}.

Thermogravimetric analysis. TGA analysis were performed using a Mettler Toledo Star System 1 equipped with a gas controller GC10. The experiments were conducted applying a ramp from 25 to 800 °C and a scan rate of 10 °C/min in air.

Scanning Electron Microscopy. SEM images were collected using Zeiss Gemini 500 scanning electron microscope, operating at 5 kV. Samples were casted on a silicon slide from 2-propanol or THF dispersion.

Adsorption isotherms. Nitrogen adsorption isotherms at 77 K were collected up to 1 bar using Micromeritics analyzer ASAP2020 HD. Samples were previously outgassed overnight at 130 °C (Zn-FTR) and 140 °C (Zr-FTR) to remove all the adsorbed species. Low temperature (77 K) nitrogen adsorption isotherms were fitted using Langmuir and BET model and surface areas were calculated in the range from 0.015 to 0.1 p/p°. Pore size distributions (PSD) were calculated according to DFT model.

Powder X-ray diffraction and structure refinement. Powder X-ray diffraction (PXRD) measurements were accomplished with a Rigaku powder diffractometer using Cu-Kα radiation, 40 kV, 15 mA over a range of 2θ = 4.0 - 70.0 with a step size of 0.02° and a scan speed of 0.3°/s. Indexing and Rietveld refinement were performed using the TOPAS-Academic-64 V6 software package.[47,48] The initial input structure used for the PXRD refinement was generated using the CASTEP code (DFT) within the Biovia Materials Studio software package. The DFT optimizations had the unit-cell restrained to the PXRD indexed cell parameters while all the molecules could be optimized. Optimizations were performed using the GGA PBE functional with Grimme's DFT-D dispersion correction, thresholds for geometry optimization and SCF convergence were chosen as 2×10^{-6} eV. The unit-cell parameters where kept fix while all the atoms where allowed to optimize. The hydrogen atoms of the DFT optimized structure were normalized to neutron diffraction distances using the normalized option in the Mercury V 3.9.[49] The unit-cell parameters were kept fix throughout the refinement process. A DFT potential energy scan, performed for the rotors of both the Zinc and Zirconium MOFs, reveals a 30° (4-fold rotation) and 60° (2-fold rotation) rotational disorder for the Zn-FTR and Zr-FTR rotors respectively. Applying these disordered models to the structures yields a symmetry of *F*-43*c* for Zn-FTR and *F*32 for Zr-FTR. Further Rietveld refinements were performed using these space-groups and the disordered models. The background was fitted and refined using a Chebyshev polynomial with 20 coefficients in the range of the PXRD trace from 5° to 60° (until 70° for Zr-FTR) 2θ and the application of baseline shift refinement. Other corrections include: Specimen Displacement, Divergence Sample Length, Absorption with Sample Thickness Shape Intensity and Specimen Tilt. The peaks were fitted using a modified Thompson-Cox-Hastings pseudo-Voigt

"TCHZ" profile. Preferred orientation was considered using a combination of March Dollase (1 0 0, 0 1 0, 0 0 1, 1 1 0, 0 1 1, 1 0 1) and an eighth order Spherical Harmonics refinement.

Single crystal XRD diffraction and crystal structure refinement. Single crystals of Zn-FTR (ZnFTR02) were synthetized under solvothermal conditions. $Zn(NO_3)_2 \cdot 6H_2O$ (148.8 mg; 0.5 mmol) and 1,3-bicyclo[1.1.1]pentanedicarboxylic acid (31.2 mg; 0.2 mmol) were dissolved in dry N,N'-DMF (30 ml) in a 100 ml vial. The solution was heated at 120 °C for 24 h and allowed to cool at room temperature. A suitable prismatic crystal was mounted on a Bruker D8 PhotonII diffractometer and the data collection was performed at 150 K. Data reduction was performed using SAINT (Bruker software, 2012) and the absorption correction was applied with the program SADABS.[50] Using Olex2[51], the structure was solved with the ShelXS[52] program using Direct Methods and it was refined with the ShelXL[53] program using Least Squares minimization.

Crystal structure determination of ZnFTR02. Crystal Data for $C_6O_{3.25}ZnH$ (*M*=189.43 g/mol): cubic, space group P-43m (no. 215), *a*= 11.949 Å, *V*= 1706.2 Å^3, *Z* = 4, *T* = 150.0 K, μ(MoKα) = 1.415 mm^{-1}, *Dcalc* = 0.741 g/cm^3, 44302 reflections measured (5.906° $\leq$ 2Θ $\leq$ 51.448°), 670 unique (R_{int} = 0.0651, R_{sigma} = 0.0137) which were used in all calculations. The final R_1 was 0.0453 (I > 2σ(I)) and wR_2 was 0.1284 (all data).

Computational details. Atomic coordinates were imported from the refined crystal structures. Only the hydrogen atoms in the frameworks were optimized as part of a periodic system by ab initio calculations. The optimizations were performed using the GGA PBE functional with Grimme's DFT-D dispersion correction, and thresholds for geometry optimization and SCF convergence were chosen as 2×10^{-6} eV. Single point energy calculations were performed using the GGA PBE functional with Grimme's DFT-D dispersion correction, and threshold for SCF convergence were chosen as 1×10^{-6} eV.

Atomic charges for Molecular Mechanics MM and Molecular Dynamics MD calculations. Single point calculations were performed using the GGA PBE functional with Grimme's DFT-D dispersion correction; thresholds for SCF convergence were chosen as 1×10^{-6} eV. The Milliken charges were calculated at the end of the SCF cycle. These atomic charges were used in all the Molecular Mechanics and Molecular Dynamics calculations.

Molecular Mechanics (MM) and Molecular Dynamics (MD) Simulations. All MM and MD calculations were performed using the Forcite-Plus module. MD simulations were performed using UFF with an Ewald summation method for both Electrostatics and van der Waals. A NPT ensemble were used at 298 K for 5 ns. The NHL thermostat (Q_{ratio} of 0.1) and Andersen barostat (Cell time constant of 5.0 ps) were used with a 1 fs time step.

Potential energy scans for the FTR conformations and rotors. Potential energy scans were performed using the GAUSSIAN16 software available through the CINECA high performance computing centre[54].

FTR dicarboxylate (COO⁻ - COO⁻) conformation. The dicarboxylate conformational scans were performed using MP2/6-311G(d) and MP2/6-311+G(d) level of theory. Initial optimization for the dicarboxylate conformation scan was performed using MP2/6-311G(d) level of theory with the rotor restrained in the crossed arrangement. Additional parameters for all calculations include a 'Ultrafine' integration grid, 'VeryTight' SCF convergence criteria with XQC algorithm and a 'Fine' optimization convergence. These methods were chosen since they work well for molecules with small changes in potential energies such as free rotating methyl moieties.[55-57] This was achieved by rotating the carboxylate groups of the FTR molecule from an angle of 90° (crossed) with respect to one another to an angle of 0° (in-plane) with an increment on 2.5°. The rotor was optimized during the scan making this a relaxed scan.

FTR rotor rotational scan. The potential energy surface (PES) scans for the FTR rotator were performed using MP2/6-311G(d), MP2/6-311+G(d) (rigid and relaxed scans) and CCSD/6-311+G(d) (rigid scan) level of theory. Additional parameters for all calculations include a 'Ultrafine' integration grid, 'VeryTight' SCF convergence criteria with XQC algorithm and a 'Fine' optimization convergence. Optimized geometries were used as input for the ROTOR potential energy scans. The rotors were scanned through 120° at 1.5° (60° at 5° increments for the CCSD method) increments following the symmetry of the FTR rotor moiety.

FTR rotor rotational scan using point charges. To evaluate the electrostatic contribution to the energy barrier of the rotator, PES scans were performed on the bicyclo[1.1.1]pentane molecule without the carboxylate moieties and capped off with hydrogen atoms. Point charges were placed at the positions of the oxygen atoms in the in-plane conformation. The point-charges were assigned ESP and NPA (NBO3) charges and the bicyclo[1.1.1]pentane rotor was then scanned relative to the plane of the point charges, like the scan for the full FTR dicarboxylate molecule. This scan yields an interaction energy that is purely electrostatic and aids in understanding the origin of the rotary barrier. The energy barrier for the crossed conformation results to be lower than 0.5 cal/mol.

^{13}C CP MAS and ^{1}H T$_1$ solid state NMR at 7 T. ^{13}C solid-state NMR experiments were carried out with a Bruker Avance 300 instrument operating at a static field of 7.04 T equipped with high-power amplifiers (1 kW) and a 4 mm double resonance MAS probe. ^{13}C{^{1}H} ramped-amplitude Cross Polarization (CP) experiments were performed at a spinning speed of 12.5 kHz using a recycle delay of 5 s and a contact time of 2 ms. The 90° pulse for proton was 2.9 µs. ^{13}C Single-Pulse Excitation (SPE) experiments were run using a 90° pulse of 4.6 µs. Quantitative solid-state ^{1}H SPE MAS NMR

spectra were performed with a Bruker Avance III 600 MHz instrument operating at 14.1 T, using a recycle delay of 20 s. A MAS Bruker probe head was used with 2.5 mm ZrO_2 rotors spinning at 30 kHz. The 90° pulse for proton was 2.9 μs. The ^{1}H chemical shift was referenced to adamantane.

^{1}H spin lattice relaxation experiments $T_1(^1H)$ at 300.13 MHz were measured using the saturation recovery pulse sequence at a spinning speed of 8 kHz in the range of 200 K - 298 K, with 32 scans for each recovery time. The 90° pulse for proton was 3.65 μs. The stability and accuracy of the temperature controller (Bruker B- VT2000) were approximately 0.1 K.

The empty materials have been characterized both under magic angle spinning (MAS) and under static conditions at 298 K and 163 K, after the activation (403 K, under vacuum, overnight). A home-made apparatus has been used for sealing the rotors in vacuo. $T_1(^1H)$ were performed in vials sealed in vacuum. I_2@Zn-FTR sample has been prepared by iodine vapor adsorption at room temperature for 72 hours.

Second moment calculation of dipolar interactions in ^{1}H static NMR spectra. The calculation of the second moment was performed using a homemade C++ version of the program proposed by Goc.[58] The program was optimized to manage large crystal cells and was able to distinguish the contribution of intra-rotor and inter-rotor interactions. The simulations were performed on a 3x3x3 supercell, with $\varphi = 3°$ and $\theta = 15°$ and were repeated multiple times, especially for the lowest number of jumps, to obtain a better averaged value. The contribution of the intra-rotor interaction is higher than 98% for the Zn compound and higher than 91% for the Zr compound.

Profile simulation of multiple spin system of rotor in ^{1}H static NMR spectra. The Zn-MOF showed a peculiar pattern of the static ^{1}H NMR spectra due to the dipolar coupling of the six hydrogens within the bicycle rotator. The bicyclopentane exhibit a six spin-half system for the hydrogens. The fitting was performed using a hydrogen nucleus distance of 1.92 Å setting the hydrogens on the vertices of a hexagon with a side of 1.92 Å, as previously studied for benzene rotation intercalated in graphite layers.[59]

Analysis of ^{13}C static NMR spectra. The static spectra were simulated with NMR-Weblab assuming $\sigma_{xx} = 44$ ppm, $\sigma_{yy} = 60$ ppm and $\sigma_{zz} = 52$ ppm with Euler angle α_0 and cone angle of 90°.[60-62]

^{1}H T_1 solid state NMR at 1.66 T, 1 T and 0.66 T. We performed ^{1}H-NMR measurements on the investigated Zn-FTR sample by means of a home-made set-up based on an Apollo spectrometer (TecMag). We generated static magnetic fields 0.66 T $\leq \mu_0 H \leq$ 1.6 T by means of an electromagnet (Bruker). The low field $T_1(^1H)$ measurements were performed on Zn-FTR sample sealed in a glass tube under a 250 torr He (6.0) atmosphere. We investigated the temperature window 4.2 K $\leq$ T $\leq$ 300 K by means of a flux cryostat (Oxford Instruments) with liquid nitrogen and liquid helium as cryogenic liquids, measuring the temperature locally by means of a thermocouple junction displaced

from the sample by ~ 5 cm. Additionally, we accessed temperatures $1.3\,\mathrm{K} \leq T \leq 4.2\,\mathrm{K}$ by means of a static cryostat (International Cryogenics) by vapour pumping over a liquid helium bath. In these conditions, in addition to the thermocouple sensor, we kept control on the temperature value also by measuring the vapour pressure over the helium bath. We prepared an ad-hoc resonant circuit composed of a coil, used to generate the alternating magnetic field and to detect the ^{1}H-NMR signal inductively, and of external variable capacitors aimed at the optimization of the tuning/matching of the overall impedance at the working frequency. We tailored the coil specifically for the sample – which was sealed in a quartz tube under inert atmosphere to avoid deterioration by air-contact – aiming at the maximization of its filling factor. We checked both on the empty quartz tube and with the empty coil that the ^{1}H-NMR signal was entirely originating from the protons within the investigated Zn-MOF sample. We quantified the spin-lattice relaxation time T_1 of the sample by means of the conventional inversion recovery radiofrequency (RF) pulsed sequence. The relaxation times where fitted using the Kubo-Tomita equation.[63]

References

47. Coelho, A.A. Indexing of powder diffraction patterns by iterative use of singular value decomposition. *J. Appl. Cryst.* **36**, 86–95 (2003).
48. Coelho, A.A. & Kern, A. Discussion of the indexing algorithms within TOPAS. *CPD Newsletter* **32**, 43-45 (2005).
49. Macrae, C. F., Bruno, I. J., Chisholm, J. A., Edgington, P. R., McCabe, P., Pidcock, E., Rodriguez-Monge, L., Taylor, R., van de Streek, J. & Wood, P. A. Mercury CSD 2.0 - New Features for the Visualization and Investigation of Crystal Structures. *J. Appl. Cryst.* **41**, 466-470 (2008).
50. Krause, L., Herbst-Irmer, R., Sheldrick G. M. & Stalke D. *J. Appl. Cryst.* **48**, 3-10 (2015).
51. Dolomanov, O. V., Bourhis, L. J., Gildea, R. J., Howard, J. A. K. & Puschmann, H. *J. Appl. Cryst.* **42**, 339-341 (2009).
52. Sheldrick, G.M. *Acta Cryst.* **A64**, 112-122 (2008).
53. Sheldrick, G.M. *Acta Cryst.* **C71**, 3-8 (2015).
54. Frisch, M. J. et al. Gaussian 16, Revision B.01, Gaussian, Inc., Wallingford CT (2016).
55. Eibl, K., Kannengießer, R., Stahl, W., Nguyen, H. V. L. & Kleiner, I. Low barrier methyl rotation in 3-pentyn-1-ol as observed by microwave spectroscopy. *Molecular Physics* **114**, 3483-3489 (2016).
56. Ilyushin, V., Rizzato, R., Evangelisti, L., Feng, G., Maris, A., Melandri, S. & Caminati, W., Almost free methyl top internal rotation: Rotational spectrum of 2-butynoic acid. *J. Mol. Spectrosc.* **267**, 186-190 (2011).
57. Zhao, Y.;, Mouhib, H., Li, G., Kleiner, I. & Stahl, W. Conformational analysis of tert-butyl acetate using a combination of microwave spectroscopy and quantum chemical calculations. *J. Mol. Spectrosc.* **322**, 38-42 (2016).
58. Goc, R. Computer calculation of the Van Vleck second moment for materials with internal rotation of spin groups. *Comp. Phys. Comm.* **162**; 102-112 (2004).
59. Panich, A. M. & Panich, E. A. NMR Lineshape of a Six-Spin System with Dipole-Dipole Interaction. Application to Benzene. *J. Magn. Reson.* **116**, 113-116 (1995).
60. Macho, V., Brombacher L. & Spiess, H. W. The NMR-WEBLAB: An internet approach to NMR lineshape analysis. *Appl. Magn. Reson.* **20**, 405-432 (2001).
61. Facelli, J. C. et al. Low-temperature carbon-13 magnetic resonance in solids. 5. Chemical shielding anisotropy of the 13CH2 group. *J. Am. Chem. Soc.* **107**, 6749-6754 (1985).

62. Pecul, M., Dodziuk, H., Jaszunski, M., Lukin, O. & Leszezynski, J. Ab initio calculations of the NMR spectra of [1.1.1]propellane and bicyclo[1.1.1]pentane. *Phys. Chem. Chem. Phys.* **3**, 1986-1991 (1985).
63. Kubo, R. & Tomita, K. A General Theory of Magnetic Resonance Absorption. *J. Phys. Soc. Jpn.* **9**, 888-919 (1954).

Data Availability

X-ray crystallographic data have been deposited at the Cambridge Crystallographic Data Centre (http://www.ccdc.cam.ac.uk/) with reference no. 1994502 (ZnFTR02), 1994503 (ZnFTR_PXRD) and 1994504 (ZrFTR_PXRD). A copy of the data can be obtained free of charge via https://www.ccdc.cam.ac.uk/structures/. All other data supporting the findings of this study are available within the Article and its Supplementary Information. Data are also available from the corresponding author upon reasonable request. Raw data are available for Figure 5.